Chemical Science

ROYAL SOCIETY OF CHEMISTRY

EDGE ARTICLE

View Article Online
View Journal | View Issue

Cite this: *Chem. Sci.*, 2024, **15**, 12606

All publication charges for this article have been paid for by the Royal Society of Chemistry

Achieving efficient and stable blue thermally activated delayed fluorescence organic light-emitting diodes based on four-coordinate fluoroboron emitters by simple substitution molecular engineering†

Panpan Li, [ab] Shiu-Lun Lai, [a] Ziyong Chen, [a] Wai Kit Tang, [a] Ming-Yi Leung, [ab] Maggie Ng, [a] Wing-Kei Kwok, [ab] Mei-Yee Chan *[ab] and Vivian Wing-Wah Yam *[ab]

Achieving both high efficiency and high stability in blue thermally activated delayed fluorescence organic light-emitting diodes (TADF-OLEDs) is challenging for practical displays and lighting. Here, we have successfully developed a series of sky-blue to pure-blue emitting donor–acceptor (D–A) type TADF materials featuring a four-coordinated boron with 2,2′-(pyridine-2,6-diyl)diphenolate (dppy) ligands, *i.e.* **1–8**. Synergistic engineering of substituents on the phenyl bridge as well as the electronic properties and the attached positions of heteroatom N-donors not only enables fine-tuning of the emission colors, but also modulates the nature and energies of their triplet excited states that are important for the reverse intersystem crossing (RISC). Particularly for the compound with two methyl substituents on the phenyl bridge (compound **8**), RISC is significantly facilitated through the vibronic coupling of the energetically close-lying triplet charge transfer (^{3}CT) and the triplet local excited (^{3}LE) states, when compared to analogue **7**. Efficient sky-blue to pure-blue OLEDs with electroluminescence peaks (λ_{EL}) at 460–492 nm have been obtained, in which *ca.* five-fold higher external quantum efficiencies (EQEs) of 18.9% have been demonstrated by **8** than that by **7**. Moreover, *ca.* thirty times longer device operational half-lifetimes (LT_{50}) of 9113 hours for **8** than that for **7** as well as satisfactory LT_{50} reaching 26 643 hours for **6** at an initial luminance of 100 cd m^{-2} have also been demonstrated. To the best of our knowledge, these results represent one of the best high-performance blue OLEDs based on tetracoordinated boron TADF emitters. Moreover, the design strategy presented here has provided an attractive strategy for enhancing the device performance of blue TADF-OLEDs.

Received 29th December 2023
Accepted 18th June 2024

DOI: 10.1039/d3sc06989c

rsc.li/chemical-science

Introduction

The development of thermally activated delayed fluorescence (TADF) materials, which can realize 100% internal quantum efficiency (IQE) by up-converting non-emissive triplet excitons to emissive singlet excitons *via* reverse intersystem crossing (RISC), has been considered as a third generation technology for organic light-emitting diodes (OLEDs).[1] Since the first report on TADF-OLEDs in 2012,[2] the research and development of TADF-OLEDs has drawn considerable attention recently.[3–5] Apart from the unity IQE and the potential for lower cost, purely organic TADF materials possess great potential for developing blue-emitting OLEDs with high efficiencies and processability suitable for full-color displays.[5–12]

From the kinetic viewpoint, a fast RISC (k_{RISC}) and a high fluorescence rate constant ($k_{r,S}$), both of which can alleviate the unwanted exciton annihilation and out-compete the non-radiative process, are favorable for high photoluminescence quantum efficiencies and long operational lifetimes of OLEDs.[13] Up to now, the predominant and effective molecular design strategy for a TADF emitter has been still the construction of a twisted donor–acceptor (D–A) configuration, in which the overlap of the highest occupied molecular orbital (HOMO) and the lowest unoccupied molecular orbital (LUMO) can be minimized, hence leading to a small singlet–triplet energy gap (ΔE_{ST}). Given a thermally accessible ΔE_{ST}, however, spin–orbit

[a]*Institute of Molecular Functional Materials and Department of Chemistry, The University of Hong Kong, Pokfulam Road, Hong Kong, P. R. China. E-mail: wwyam@hku.hk*

[b]*Hong Kong Quantum AI Lab Limited, 17 Science Park West Avenue, Pak Shek Kok, Hong Kong, P. R. China*

† Electronic supplementary information (ESI) available: Experimental details, synthesis and characterization, thermogravimetric analysis, photophysical properties, TADF properties, electrochemical studies, computational studies and device fabrication and characterization. See DOI: https://doi.org/10.1039/d3sc06989c

coupling (SOC)-mediated spin-flipping process from charge transfer triplet (^{3}CT) to singlet (^{1}CT) excited states in purely organic materials is inefficient.[14] Recent studies have shown that RISC can be accelerated by a second-order vibronically coupled mechanism, in which the SOC between ^{1}CT and ^{3}CT is greatly enhanced by a vibronic coupling of the energetically close-lying ^{3}CT state and the triplet local excited (^{3}LE) state.[15–23] Unfortunately, in terms of the fluorescence radiation from the lowest singlet excited state (S_1) to the ground state (S_0), a small HOMO–LUMO overlap corresponds to a small transition probability from HOMO to LUMO resulting from a small oscillator strength, and hence usually results in a low photoluminescence quantum yield (PLQY). As a result, a careful manipulation on the trade-off between a small ΔE_{ST} and a high PLQY is also of prime importance.

The electron-accepting nature of tricoordinate boron moieties, together with their interesting luminescence properties,[24–27] have enabled them to be promising acceptor motifs for constructing blue-emitting D–A structured TADF materials as well as boron-embedded multi-resonance (MR) TADF materials.[28–32] Particularly, in order to weaken the electron-withdrawing ability of a tricoordinate boron for realizing deeper blue emissions, embedding boron atom into heteroatom-bridged or heteroatom donor-based chelating ligands has been demonstrated to be an effective design approach.[33–35] For instance, upon replacing the B–C bond with the B–O bond, a considerable blue shift of 29 nm (1357 cm^{-1}) in the photoluminescence spectra has been demonstrated in a borinate-ester-based TADF emitter, when compared with the isostructural phenoxaborin-based analogue.[34,35] The blue-shifted emission is originated from the electron donation of the oxygen atom to boron that lowers the electron-accepting ability on the boron atom. Despite encouraging external quantum efficiencies (EQEs >30%) of tricoordinate boron-based TADF-OLEDs,[36–39] still, the synthesis is challenging and the device operational stability is unsatisfying,[38,39] predominantly due to the intrinsic instability of the tricoordinate boron center.[28] On the contrary, upon complexation of a Lewis base to the tricoordinate boron center, the Lewis acid–base interaction can stabilize the resultant tetracoordinate boron in an inert-gas configuration and thus improve the chemical stability.[40–52] These, together with the facile synthesis and modification of the tetracoordinate borate-based TADF emitters, would render them as promising candidates for both efficient and stable TADF-OLEDs.[53] Nonetheless, to date, only a few blue-emitting four-coordinate boron-based TADF materials with EQEs approaching 16% have been reported,[39,40,54–58] probably due to an effective π-conjugation in the structurally constrained tetracoordinate boron moieties and thus a stabilized LUMO induced red-shifted emission.[53]

Previously, our group reported a blue TADF material, 4-DTC-Ph(dppy)BF (Fig. 1a), in which a 3,6-di-*tert*-butylcarbazole (DTC) donor and a 2,2′-(pyridine-2,6-diyl)diphenolate (dppy) fluoroboron ((dppy)BF) acceptor was bridged by a phenyl linker.[50] The findings revealed that the nature of S_1 and the lowest triplet excited state (T_1) were ^{1}CT and ^{3}LE on the (dppy)BF moiety, respectively. In light of the aforementioned scenarios, it is envisaged that a delicate tuning of the CT state energy of (dppy)BF-based TADF emitters, which could be realized by modulating the donor strength of the N-donor and the donor–acceptor conformation, could lead to a control of both the frontier orbital distribution and the relative energy order and levels of the ^{3}CT and ^{3}LE state. Particularly for **6**, the attachment of two DTC at the *para*-position of the phenolate moieties not only allows us to investigate the donor–acceptor conformation-modulated excited states, but also guarantees the electrochemical stabilities of both the carbazole and the phenolate moieties.[58,59] Herein, we have designed and synthesized a series of (dppy)BF-based TADF emitters *via* the π-bridge engineering and the N-donor modulation, *i.e.* **1–8**, targeting high-quality blue emissions as well as high electroluminescence quantum efficiencies (Fig. 1). High emission energies can be realized through the removal of the π-bridge (**1**), the simple methyl substitution engineering on the phenyl bridge (**2**, **3** and **8**) and the utilization of a weaker N-donor (**5**). Moreover, energetically close-lying T_1 state (^{3}CT) and T_2 state (^{3}CT and ^{3}LE for **6** and **8**, respectively) with the energy difference ($\Delta E_{T_1-T_2}$) of 0.02 eV for **6** and 0.06 eV for **8** are determined by computational studies, respectively, by which an accelerated RISC process through a second-order vibronically coupled mechanism can be anticipated. Pure-blue OLEDs with a maximum EQE of 7.7% at a λ_{EL} of 468 nm and CIE coordinates of (0.15, 0.18), and sky-blue OLEDs with a maximum EQE of 18.9% at a λ_{EL} of 492 nm and CIE coordinates of (0.18, 0.42) have been demonstrated by compounds **3** and **8**, respectively. Further boosted device performance with an EQE reaching 20.8% has been achieved by **8** at a dopant concentration of 14 v/v%. More impressively, long half-lifetimes (LT_{50}) at a L_0 of 100 cd m^{-2} of 918 hours and 26 643 hours for pure-blue and sky-blue OLEDs have been achieved, respectively. The synergistic effects of an appropriate frontier orbital overlap and an efficient spin-vibronic coupling mediated RISC have been demonstrated to contribute to these record-high device efficiencies and operational stabilities.

Synthesis and characterization

The halogenated 2,6-bis(2-methoxyphenyl)pyridines were prepared according to modifications of literature procedures,[50,60] which were subsequently allowed to react with the corresponding diarylamines *via* Buchwald–Hartwig coupling reactions. Further demethylation by pyridinium chloride (py·HCl) and coordination with boron trifluoride diethyl etherate ($BF_3 \cdot OEt_2$) afforded the target compounds **1–8** (Fig. S1†). The corresponding synthetic routes are provided in Fig. S1.† The identities of **1–8** have been fully confirmed by ^{1}H, ^{19}F{^{1}H} and ^{11}B{^{1}H} NMR spectroscopy, high resolution electron ionization (EI) or electrospray ionization (ESI) mass spectrometry as well as elemental analyses. All the fluoroboron compounds are revealed to be thermally stable by thermogravimetric analysis (TGA) (Fig. S2 and Table S1†), suggesting their potentials for the fabrication of vacuum-deposited devices.

Steady-state photophysical properties

The UV-vis absorption and emission spectroscopy of **1–8** in toluene solutions and in doped thin films have been carried out

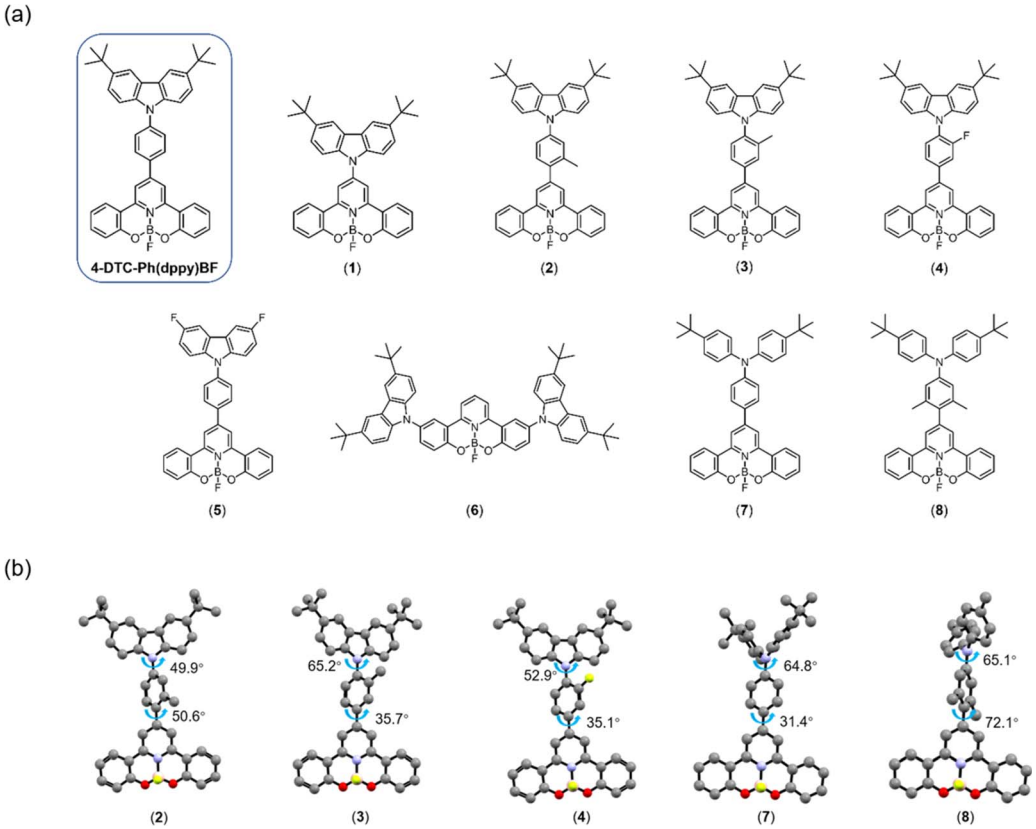

Fig. 1 (a) Chemical structures of the previously reported 4-DTC-Ph(dppy)BF[50] and the newly developed compounds **1–8**. (b) Optimized S_0 geometries of representative compounds **2–4**, **7** and **8** labeled with dihedral angles.

to investigate their basic photophysical properties (Fig. 2, Tables 1 and S2†). With reference to the absorption studies of (dppy)BF (Fig. S3†) and 4-DTC-Ph(dppy)BF,[50] the high-energy vibronically structured absorption bands of **1–8** at *ca.* 310–360 nm are tentatively assigned as π–π* transitions of the respective (dppy)BF moieties and the low-energy absorption bands beyond 360 nm are assigned as an intramolecular charge transfer (ICT) transition from the respective N-donor moiety to the (dppy)BF acceptor moiety, with some mixing of π–π* transitions. Compared to 4-DTC-Ph(dppy)BF,[50] removing the π-bridge in **1** leads to a hypsochromic shift in the low-energy absorption band maximum from 386 nm to 377 nm. This can be ascribed to a reduced π-conjugation length in **1** and thus an enlarged π−π* energy gap. Comparing **2–4**, the introduction of an *ortho*-substituent relative to (dppy)BF in **2** gives rise to a blue shift in the low-energy absorption band, whereas the introduction of an *ortho*-substituent relative to DTC, regardless of its electronic properties, in **3** and **4** gives rise to a similar absorption profile. Such observations can be rationalized by the frontier orbital distribution, in which the HOMO is primarily localized on the π orbital of DTC and the LUMO is primarily localized on the π* orbital of (dppy)BF and its adjacent methyl-substituted phenyl ring. Accordingly, the *ortho*-substitution relative to the DTC moiety has a negligible effect on the HOMO, whereas the *ortho*-substitution relative to the (dppy)BF moiety would cause a reduction in the electron delocalization and

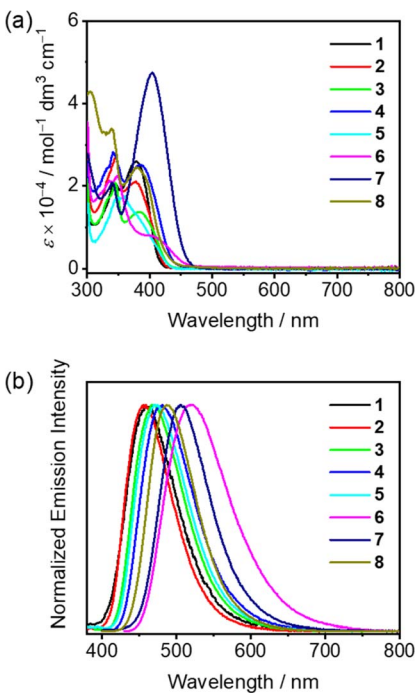

Fig. 2 (a) Electronic absorption spectra, and (b) normalized emission spectra of **1–8** in toluene solution (10^{-5} M).

Table 1 Key photophysical properties of 4-DTC-Ph(dppy)BF[50] and **1–8** at room temperature

	Solution						Thin film[f]			
Compound	λ_{em}/nm	Φ/%	τ[a]/ns	$k_{r,S}$[c]/10^8 s^{-1}	$k_{nr,S}$[d]/10^8 s^{-1}	ΔE_{ST}[e]/eV	λ_{em}/nm	Φ/%	τ_p/ns	τ_d/μs
1	461	18[a]/21[b]	5.1	0.35	1.33	0.42	461	43	4.7	125
2	457	30[a]/33[b]	4.9	0.61	1.24	0.38	459	53	9.5	359
3	469	23[a]/27[b]	3.5	0.66	1.78	0.36	466	47	7.0	287
4	481	13[a]/17[b]	3.8	0.34	1.67	0.31	478	78	5.0	143
5	472	21[a]/22[b]	3.4	0.62	2.19	0.36	451	36	4.9	377
6	520	19[a]/24[b]	7.9	0.24	0.76	0.25	500	53	10.3	559
7	506	71[a]/82[b]	4.4	1.61	0.35	0.15	515	99	7.1	12.7
8	488	53[a]/66[b]	5.2	1.02	0.53	0.22	492	94	5.3	38.9
4-DTC-Ph(dppy)-BF	468	31[a]/39[b]	3.1	1.00	1.56		468	71	5.4	453

[a] Measured in aerated toluene solution with a concentration of 10^{-5} M. [b] Measured in degassed toluene solution with a concentration of 10^{-5} M. [c] Rate constant of fluorescence radiative decay ($S_1 \rightarrow S_0$): $k_{r,S} = \Phi_p/\tau$. [d] Rate constant of nonradiative decay ($S_1 \rightarrow S_0$): $k_{nr,S} = ((1-\Phi)/\Phi) \times k_{r,S}$. [e] $\Delta E_{ST} = E_{S1} - E_{T1}$ (see ESI for details). [f] Measured in 5 wt% doped mCP thin films.

destabilize the LUMO. Similarly, comparing **7** and **8**, which have the same 4,4′-di-*tert*-butyldiphenylamine (DTDPA) donor moiety, the di-*ortho*-methyl-substitution on the phenyl bridge relative to the (dppy)BF acceptor in **8** leads to an obvious hypsochromic shift in the low-energy absorption band, that is, 405 nm for **7** and 380 nm for **8**. Such observations are further supported by computational studies (see ESI†), in which the dihedral angle between the (dppy)BF unit and its adjacent aryl rings increases from *ca.* 35° in **3** and **4** to *ca.* 50° in **2** and from *ca.* 31° in **7** to *ca.* 72° in **8** respectively (Fig. 1b). Besides, the molar extinction coefficient (ε) of **7** is more than two-fold higher than that of **8**, resulting from a relatively planar molecular structure and thus a better HOMO–LUMO overlap in **7**. Meanwhile, the low-energy absorption band is also found to be sensitive to the electron-donating ability of the N-donor moiety, in which a considerable red shift from 360 nm to 401 nm to 405 nm is observed when comparing **5** with a 3,6-difluorocarbazole (DFC) donor to **6** with two DTC donors to **7** with a DTDPA donor. Such assignments can be further supported by time-dependent density functional theory (TDDFT) calculations (see ESI† for details). These results suggest that both the strength and the degree of twisting of the N-donor moiety play an important role in controlling the energy and the nature of the lowest-lying excited states, which in turn could govern the TADF properties.

Upon photoexcitation in toluene solution, all the compounds display structureless emission bands (Fig. 2b). This, together with the linear relationship between the Stokes shift and the solvent polarity suggest an ICT emissive excited state origin (Fig. S4–S6†). Consistent with the trend observed in the electronic absorption studies, the emission energies are found to be both sensitive to the extent of the π-conjugation and the electron-donating strength of the N-donor. In 5 wt% **1–8** doped 1,3-bis(carbazol-9-yl)benzene (mCP) thin films, except for **5** and **6** which show a considerable blue shift in the emission maxima, *i.e.* 21 nm (987 cm^{-1}) for **5** and 20 nm (769 cm^{-1}) for **6**, all the other compounds exhibit similar photoluminescence behaviors as observed in toluene solutions (Fig. S7†). Particularly, the blue shift in the emission spectra of **5** and **6** doped thin films is possibly arising from the restricted excited-state structural relaxation in the solid-state thin film.

Time-resolved photoluminescence studies

To verify the TADF properties of **1–8**, the time-resolved photoluminescence (PL) characteristics in the solution state and in the solid-state thin films have been investigated (Fig. 3, 4, S8 and S9†). A nanosecond emission lifetime is found for all the compounds **1–8** in aerated toluene at room temperature. Identical PL profiles with slightly higher PLQYs in degassed solutions with respect to those in aerated solutions have been revealed (Fig. S10† and Table 1). In contrast, the time-resolved PL decay characteristics of all the compounds in 5 wt% doped mCP thin films exhibit both nanosecond-order and microsecond-order decays. Moreover, the microsecond-order components for all the doped thin films show an increase upon increasing the temperature from 77 K to 300 K (Fig. 3 and S8†), typical of TADF characteristics.[2] Meanwhile, much enhanced PLQYs are observed in the doped thin films relative to those in the degassed solutions. Notably, changing the N-donor from DTC in 4-DTC-Ph(dppy)BF and **1–6** to DTDPA in **7** and **8** leads to a rather shortened emission decay lifetime (tens of microseconds) and a much higher PLQY (≥94%) in the corresponding doped thin films. Particularly, compared to **7**, the introduction of two methyl substituents on the phenyl bridge in **8** leads to a significant increase in the delayed emission component (Fig. 3 and S8†), suggesting an efficient TADF process. Nevertheless, for all the compounds, the more pronounced TADF properties in the solid-state thin film than those in the solution state can be mainly attributed to restricted intramolecular motion and thus suppressed nonradiative deactivation, both enhancing radiative decay *via* fluorescence,[61] making both intersystem crossing (ISC) and RISC processes more ready to occur.[62,63]

To gain insights into the nature of the S_1 and T_1 states, time-resolved PL spectra of **1–8** in toluene matrix at 77 K have been recorded. Specifically, the fluorescence spectra of all the compounds generally display structureless emission bands (Fig. 4 and S9†). For the phosphorescence spectra, compounds

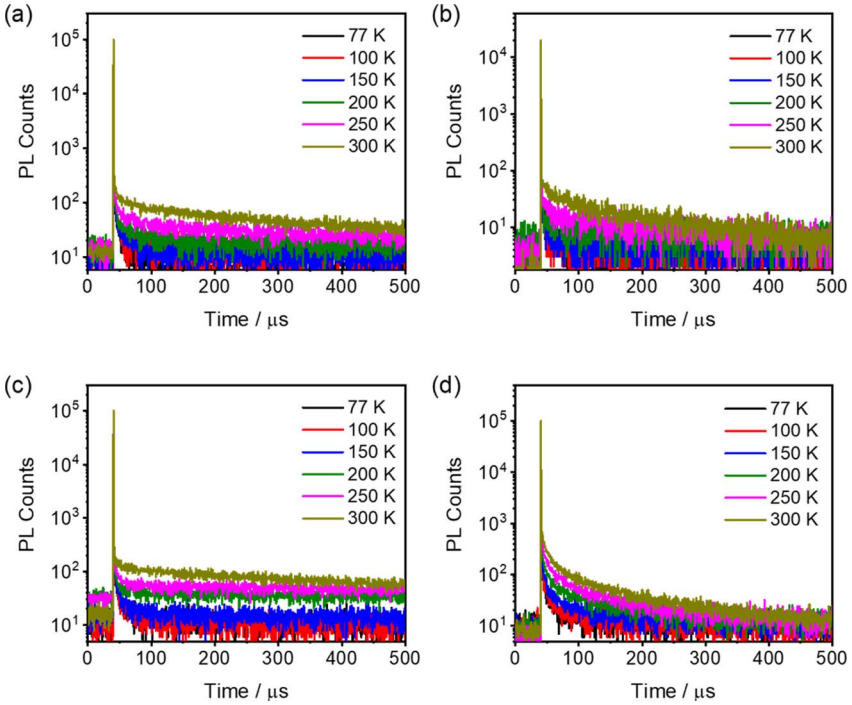

Fig. 3 Temperature-dependent PL decay curves of thin films of 5 wt% (a) **3**, (b) **4**, (c) **6** and (d) **8** doped mCP thin films.

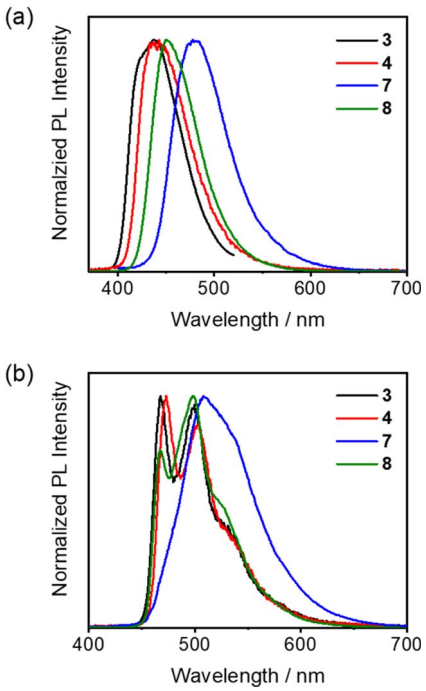

Fig. 4 Time-resolved (a) fluorescence (delay time: 0 ns) and (b) phosphorescence (gate time: 0.5–100 ms) spectra of **3**, **4**, **7** and **8** measured in toluene matrix at 77 K.

1–**5** and **8** exhibit characteristic vibronic structures of the (dppy)BF acceptor moiety (Fig. S11†), indicating that the emission predominantly stems from a ^{3}LE excited state on the (dppy)BF acceptor. As for compound **6**, a structureless phosphorescence band is observed, suggesting a charge transfer T_1 (^{3}CT) excited state origin. Notably, compared to **8**, the phosphorescence spectrum of **7** shows a less obvious vibronic feature, which might indicate a different emission origin.[16,19] Taking a closer look at the character and energies of T_1 and T_2 states for **7** and **8**, the less obvious vibronic-structured phosphorescence spectrum of **7** can be attributed to the predominant charge transfer character (73%) of T_1 as well as the large energy difference between T_1 and T_2 ($\Delta E_{T_1-T_2}$: 0.34 eV), whereas the negligible $\Delta E_{T_1-T_2}$ (0.06 eV) as well as the predominant charge transfer character of T_1 (80%) and locally excited state character of T_2 (88%) have been computed for **8** (Table S6† and see Computational studies). The vibronic-structured phosphorescence spectrum of **8** might be attributed to larger transition intensity from ^{3}LE → S_0 emission than that of ^{3}CT → S_0 emission. Considering the fact that the most relaxed CT state might not be formed at 77 K, the S_1 energies have been estimated from the fluorescence spectra recorded at 298 K, and T_1 energies was estimated from the phosphorescence spectra recorded at 77 K (Table S3†). The rather larger discrepancy between the experimental ΔE_{ST} (0.15 eV) and the computational ΔE_{ST} (0.46 eV) for **7** is likely introduced by the difference in the dihedral angle between the phenyl ring attached to the diarylamino moiety and the pyridine ring at 77 K from that of the optimized geometry of **7** from computational studies. This can be further supported by the better agreement of the experimentally determined ΔE_{ST} (0.22 eV) and the computational ΔE_{ST} (0.13 eV) for **8** where the two *ortho*-methyl substituents on the phenyl ring attached to the diarylamino moiety would restrict the rotational degrees of freedom to be similar to that of the optimized geometry from computational studies.

Transient absorption studies

In order to reveal the excited-state dynamics, nanosecond transient absorption (TA) studies have been performed on structurally similar analogues **7** and **8** in degassed toluene solution at room temperature using a 355 nm nanosecond pulsed laser (Fig. S13b† and 5). The picosecond TA spectra of **7** in degassed toluene solution at room temperature have also been recorded using a picosecond mode-locked laser (Fig. S13a†). Generally, a negative absorption band at *ca.* 520 nm and an intense and broad positive band in the region of 600–850 nm of **7** are observed in the ps-TA spectra.[64] A similar broad positive absorption band in the region of *ca.* 600–800 nm is also observed in the ns-TA spectra of **7** (Fig. S13b†). The decay constant of the negative band (3.6 ns, Fig. S13a†) is comparable to its fluorescence lifetime in toluene (4.4 ns, Table 1). This, together with the ground state non-absorbing properties of **7** in this region (Fig. 2a), suggest the negative band originates from interference from background fluorescence of **7**, which has the highest prompt fluorescence PLQY among this series of compounds.[65] On the other hand, an intense and broad positive absorption band at 400–800 nm is found in the ns-TA spectra of **8** (Fig. 5). The positive TA bands for both **7** and **8** correspond to excited state absorption (ESA).[65–68] Due to the strong laser-induced emission in the ns-TA spectra of **7** at *ca.* 460–540 nm, the ESA signals in that region is heavily masked and the exact wavelength cannot be deconvoluted. With reference to the structurally related boron-containing[69] and diphenylamine-based small molecules,[70] the ESA bands in the region of *ca.* 540 nm for **8** could be tentatively assigned to the absorption of the radical anion of the dppy-chelating boron moiety, while the ESA bands in the region of 600–800 nm for **7** and at *ca.* 680 nm for **8** could be assigned to the absorption of the radical cation of the diphenylamine moiety, respectively. The spectral shifts in the ESA bands of radical anions and cations for **7** and **8** could be ascribed to the substituent effect. Particularly, the short-lived TA signals decay in the nanosecond scale for **7** (Fig. S13a†) suggest that a vast majority of singlet excited states are deactivated *via* emission rather than ISC to the triplet state.[64,71] In contrast, for **8**, the broad ESA bands at 400–800 nm decay in the microsecond regime (Fig. 5), indicative of the involvement of the triplet state for a possible occurrence of TADF. This suggests that a large proportion of the singlet excited states undergoes ISC into the triplet manifold instead of prompt fluorescence radiative decay in **8**.[71] Notably, these findings in the TA studies of **8** can be well explained by a relatively smaller ΔE_{ST} of 0.22 eV as demonstrated by the time-resolved PL studies (Table 1 and S3†) as well as a larger SOC constant of 0.45 cm^{-1} between S_1 and T_1 as revealed by the computational studies (Table 2), as compared to the ΔE_{ST} of 0.46 eV and the SOC of 0.42 cm^{-1} of **7**, respectively.

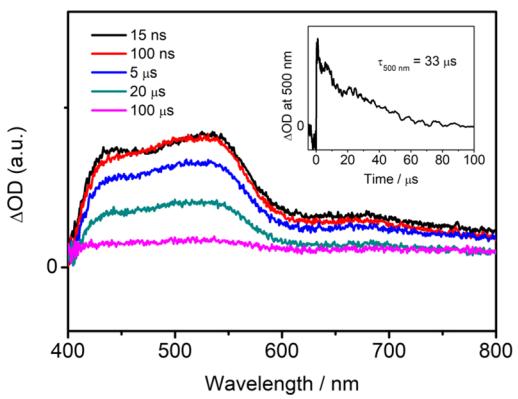

Fig. 5 Nanosecond transient absorption spectra of **8** in degassed toluene at 298 K and the decay trace monitored at 500 nm in the inset.

Computational studies

To gain further insights into the excited states involved in the TADF process, the S_1 and T_1 excited states for compounds **1–8** have been optimized with the time-dependent density-functional theory (TDDFT) at PBE0 level of theory. It is found that the lowest energy transitions in the optimized S_1 and T_1 structures of **1–8** are contributed by HOMO → LUMO excitation. In the S_1 state, their HOMOs are predominantly the π orbitals localized on the N-donor, while the LUMO is the π* orbital of the (dppy)BF moiety (Fig. S23†). Therefore, the S_1 excited states of **1–8** can be assigned as the ^{1}ICT [π(N-donor) → π*((dppy)BF)] state. Increasing the donor strength of the N-donor from one DTC in 4-DTC-(dppy)BF to two DTC in **6** and one DTDPA in **7** destabilizes the HOMO, which in turn lowers the energy of the CT states; whereas introducing two methyl-substituents on the phenyl bridge in **8** stabilizes the HOMO and hence the CT states with respect to that in **7** with the same DTDPA donor moiety (Fig. S26†), in good agreement with the emission studies (Table 1). In the T_1 state, the frontier orbitals of **4** and **6–8** share the same nature as that in the S_1 state, and can be assigned as originating from the ^{3}ICT state. For **1–3** and **5** in the T_1 state, the HOMOs and LUMOs are mainly the π and π* orbitals of the (dppy)BF moiety (Fig. S24†), therefore can be assigned as the ^{3}LE [π → π*((dppy)BF)] state. Notably, the alteration of the nature of the T_1 state in **6–8** (^{3}CT) as compared to that in 4-DTC-(dppy)BF (^{3}LE)[50] has been attributed to the strong donor strength of the N-donor in **6–8**, which would effectively stabilize the ^{3}CT state with the corresponding energy lower than that of the ^{3}LE state.

Table 2 Computed spin–orbit coupling constants between singlet and triplet excited states and norm of derivative couplings between triplet excited states for **6–8**

Compound	ΔE_{ST}/eV	$\Delta E_{T_1-T_2}$/eV	$SOC_{S_1-T_1}$/cm^{-1}	$SOC_{S_1-T_2}$/cm^{-1}	$DC_{T_1-T_2}$/$bohr^{-1}$
6	0.25	0.02	0.44	0.23	29.1
7	0.46	0.34	0.42	0.46	1.2
8	0.13	0.06	0.45	0.56	1.0

The spin-flipped up-conversion from the T_1 to S_1 state is influenced by direct SOC (*i.e.*, $SOC_{S_1-T_1}$), spin-vibronic interactions *via* higher-lying triplet states and the ΔE_{ST} value. The smallest ΔE_{ST} of 0.13 eV for **8** is consistent with experimentally observed strongest TADF characteristic among **6–8**. The moderate $SOC_{S_1-T_1}$ in the range of 0.42–0.45 cm^{-1} for **6–8** suggests that the direct SOC contribution is similar among them. To explore the potential involvement of spin-vibronic interactions in the TADF process, the SOC and derivative couplings (DC) associated with the second lowest-energy triplet excited state (T_2) in **6–8** have been computed (Table 2). Theoretical analysis has demonstrated that large $SOC_{S_1-T_2}$ and $DC_{T_1-T_2}$ along with small $\Delta E_{T_1-T_2}$ values can facilitate $T_1 \rightarrow S_1$ RISC *via* T_2 state.[72] The computed $SOC_{S_1-T_2}$ values are in the same order of magnitude for **6–8**. However, results from interfragment CT (IFCT) analysis indicate that T_2 states exhibit different dominant characters, specifically ^{3}CT, ^{3}LE, and ^{3}LE for compounds **6–8**, respectively, with corresponding $\Delta E_{T_1-T_2}$ gaps of 0.02, 0.34, and 0.06 eV. The rather small $\Delta E_{T_1-T_2}$ values for **6** and **8** are indicative of a strong vibronic coupling between the T_1 and T_2 states that has been demonstrated to facilitate RISC (Fig. S27†),[15–23] whereas such a vibronic coupling is diminishingly small for **7** given its large $\Delta E_{T_1-T_2}$. Furthermore, the large $DC_{T_1-T_2}$ value for compound **6** provides additional acceleration for RISC as compared to **7**. All these computational results have supported the effectiveness of the present design strategies of regulating the N-donor strength and the donor–acceptor conformation to modulate the CT energy level for fine color tuning as well as to alter the relative energy order and levels of the ^{3}CT and ^{3}LE states for an efficient RISC.

OLED fabrication and characterization

The electroluminescence (EL) properties of **1–8** in vacuum-deposited OLEDs with different device configurations (device A and device B) have been investigated (see ESI† for details). The EL characteristics of **1–8** at different dopant concentrations (*i.e.* $x = 2$, 5, 8, 11, and 14 v/v%) are shown in Fig. 6 and S29–S32,† and the corresponding data are summarized in Table S8.† Notably, 3,3′-di(9*H*-carbazol-9-yl)biphenyl (*m*-CBP) has been used as the host material due to its higher thermal stability than mCP, favoring a higher operational stability of OLEDs. Consistent with the PL spectra of doped thin films, all devices fabricated with **1–8** exhibit Gaussian-shaped EL bands (Fig. 6a, S29 and S30†). With the same device structure, higher EL energies are obtained *via* the simple introduction of methyl substituents on the phenyl bridge when comparing **2** to 4-DTC-Ph(dppy)BF[50] as well as **8** to **7**, respectively (Table S8†). On the other hand, despite the different device structures, the EL energies are generally observed to be in order of **5** > **6** > **7** and are in good agreement with the trend of electron-donating strength of the N-donor. Moreover, relatively small FWHMs from 60 nm to 72 nm with spectral shifts of ~181, 553, 359, 706 and 184 cm^{-1} are observed for the blue-emitting devices based on **1–5** with the dopant concentration from 2 v/v% to 14 v/v%, respectively. The narrow FWHMs together with the small spectral shifts are highly desirable for blue emitters to be used for displays and solid-state lighting systems.

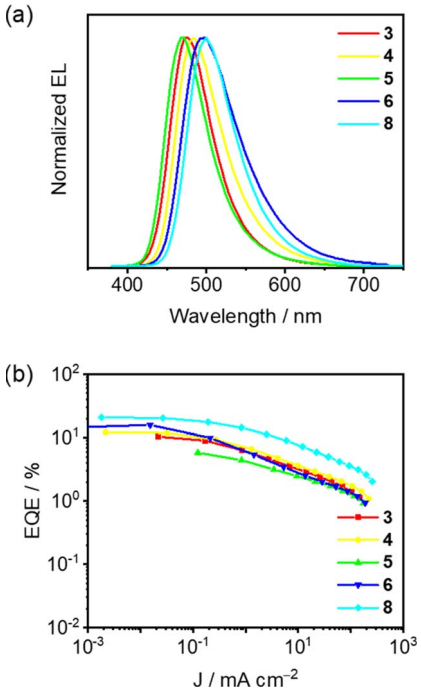

Fig. 6 (a) Normalized EL spectra and (b) EQE–current density (J) plots of the vacuum-deposited OLEDs (device B) based on 14 v/v% **3–6** and **8**.

Besides the fine-tuned blue EL, promising EQEs of as-fabricated OLEDs have also been demonstrated (Fig. 6b, S31 and S32†). Particularly, a rather low maximum EQE of 3.8% with CIE coordinates of (0.14, 0.20) for devices based on **1** can be reasonably attributed to its large ΔE_{ST}. With the same device architecture, a higher EQE of 7.7% for OLEDs fabricated with **2** than 4.3% with 4-DTC-Ph(dppy)BF[50] in the pure-blue region ($CIE_x \leq 0.15$, $CIE_y \leq 0.20$) have been achieved. On the other hand, synergistically increasing the donating strength of the N-donor and modulating the donor–acceptor conformation can also result in high performances of blue OLEDs. Particularly, a maximum EQE of 13.3% with CIE coordinates of (0.20, 0.37) for **6**-fabricated OLEDs has been demonstrated. Moreover, an EQE of 9.3% with CIE coordinates of (0.17, 0.35) for **8**-fabricated OLEDs has been obtained, more than two-fold enhancement than an EQE of 3.6% with CIE coordinates of (0.16, 0.38) for **7**. Further optimization of devices made with **8** by employing TSPO1 as the hole blocking layer at the cathode side instead of TCTA as the electron blocking layer at the anode side has led to a higher EQE of 17.0% with CIE coordinates of (0.18, 0.38) for blue OLEDs and 19.4% with CIE coordinates of (0.20, 0.47) for sky-blue OLEDs, which are presumably due to a more balanced charge carrier transport within devices.[73] For fair comparison, 4-DTC-Ph(dppy)BF-based OLEDs employing TSPO1 as the exciton blocking layer have also been fabricated, in which maxima EQEs of 14.6% with CIE coordinates of (0.16, 0.29) have been obtained. Particularly, current and power efficiencies of the 14 v/v% device based on **8** (*i.e.* 57.9 cd A^{-1} and 60.6 lm W^{-1}) are almost double those of the device based on 4-DTC-Ph(dppy)BF (*i.e.* 27.8 cd A^{-1} and 29.1 lm W^{-1}), corresponding to a high EQE of 20.8%.

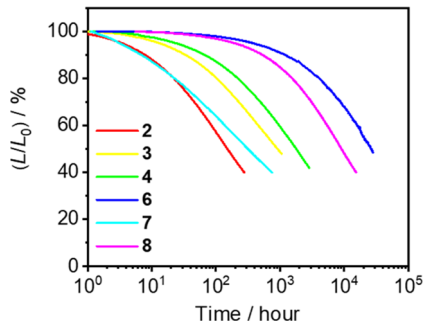

Fig. 7 Relative luminescence (L/L_0) of vacuum-deposited OLEDs based on **2**–**4** and **6**–**8** as a function of time at a constant driving current density of 20 mA cm^{-2}.

Table 3 Operational stabilities of vacuum-deposited devices made with **2**, **3** and **6**–**8**

		Lifetime/hours	
Compound	L_0/cd m^{-2}	LT_{50}[a] @ L_0[b]	LT_{50} @ 100 cd m^{-2}
2	745	5	151
3	1140	15	918
4	1206	26	1792
6	1374	310	26 643
7	1269	4	317
8	3010	28	9113

[a] LT_{50} is defined as the operational lifetime at 50% of initial luminance. [b] L_0 is defined as the initial luminance.

The operational stabilities of the vacuum-deposited devices based on **2**–**4** and **6**–**8** have also been investigated by accelerated testing at a constant driving current density of 20 mA cm^{-2}. The relative luminance of the OLEDs based on **2**–**4** and **6**–**8** as a function of time is depicted in Fig. 7 and the corresponding data are summarized in Table 3. Devices fabricated with **2**–**4** and **6**–**8** have achieved half-lifetimes LT_{50} of 151, 918, 1792, 26 643, 317 and 9113 hours, respectively, at an initial brightness (L_0) of 100 cd m^{-2}. Operational lifetimes of devices fabricated with **6** and **8** show tens of times longer than those for **2**, **3** and **7**, and four to ten times longer than that for 4-DTC-Ph(dppy)BF,[50] respectively. Besides, the better electrochemical stability of the *para*-substituted phenolate moieties might also contribute the superior device operational lifetimes of **6**. It should also be highlighted that both the device quantum efficiencies and operational stabilities of **8** demonstrated in this work represent one of the highest values among the state-of-the-art blue-emitting TADF-based OLEDs with similar emission wavelengths or CIE coordinates (Table S9†).

Conclusions

In summary, a series of sky-blue to pure-blue dppy-chelated fluoroboron TADF materials has been developed and utilized as dopants for OLED applications. Both the electronic nature and the position of the substitution on the phenyl bridge and the N-donor appended to the (dppy)BF acceptor can effectively alter and fine-tune their electronic structures and photophysical properties. Particularly, for emitters **7** and **8** with the same DTDPA N-donor, the simple methyl substitution engineering on the phenyl bridge in **8** destabilizes both the ^{1}CT (S_1) state for a higher emission energy and the ^{3}CT (T_1) state that brings its energy closer to that of the ^{3}LE (T_2) state for an efficient RISC *via* a spin-vibronic coupling mechanism. Sky-blue to pure-blue vacuum-deposited OLEDs fabricated with these boron emitters have achieved maxima EQEs of 18.9%. Moreover, further boosted device performance with an EQE of 20.8% has been demonstrated by **8** at a higher dopant concentration. Importantly, satisfactory half-lifetimes of 918 hours for pure-blue OLEDs and long half-lifetimes of 26 643 hours for sky-blue OLEDs have been realized. The synergistic engineering of the substitution on the π-bridge and the nature of the N-donor is believed to be of great importance toward future development of robust blue TADF materials based on four-coordinate borates and other bipolar D–A systems.

Notes

Materials and reagents

Bis(4-(*tert*-butyl)phenyl)amine and 3,6-di-*tert*-butyl-9*H*-carbazole were purchased from TCI or AK Scientific, Inc. Pyridine hydrochloride (Py·HCl) and boron trifluoride diethyl etherate ($BF_3 \cdot OEt_2$) were available from Sigma-Aldrich. All solvents were purified and distilled using standard procedures before use. Toluene (≥99.8%, SPECTRONORM for spectroscopy) was purchased from VWR Chemicals. Tetra-*n*-butylammonium hexafluorophosphate (Aldrich, 98%, $^nBu_4NPF_6$) was recrystallized for no less than three times from hot absolute ethanol prior to use. All other reagents were of analytical grade and were used as received. All reactions were performed under anaerobic and anhydrous conditions using standard Schlenk techniques under an inert atmosphere of nitrogen.

Data availability

The datasets supporting this article have been uploaded as part of the ESI.†

Author contributions

V. W.-W. Y. initiated and designed the research. V. W.-W. Y. and P. L. designed the boron compounds. P. L. conducted the synthesis, characterization, photophysical and electrochemical measurements of the boron compounds. M.-Y. L. and W.-K. K. carried out the transient absorption measurements and data analysis. Z. C., W. K. T. and M. N. performed and analyzed the computational calculations. S.-L. L. and M.-Y. C. carried out the OLED fabrication and characterizations. P. L., Z. C., W. K. T., M.-Y. C. and V. W.-W. Y. wrote the manuscript. V. W.-W. Y. supervised the work. All authors discussed the results and contributed to the final manuscript.

Conflicts of interest

There are no conflicts to declare.

Acknowledgements

V. W.-W. Y. acknowledges support from The University of Hong Kong (HKU). The work described in this paper was supported by the Hong Kong Quantum AI Lab Ltd under the AIR@InnoHK cluster of the Innovation and Technology Commission (ITC). The computations were performed using research computing facilities offered by the Information Technology Services at HKU. We acknowledge Prof. Chi-Chiu Ko and Dr Shun-Cheung Cheng of the City University of Hong Kong for their helpful discussion in the transient absorption spectroscopic studies.

References

1 G. Hong, X. Gan, C. Leonhardt, Z. Zhang, J. Seibert, J. M. Busch and S. Bräse, *Adv. Mater.*, 2021, **33**, 2005630.
2 H. Uoyama, K. Goushi, K. Shizu, H. Nomura and C. Adachi, *Nature*, 2012, **492**, 234–238.
3 X. Liang, Z.-L. Tu and Y.-X. Zheng, *Chem.–Eur. J.*, 2019, **25**, 5623–5642.
4 X. Yin, Y. He, X. Wang, Z. Wu, E. Pang, J. Xu and J.-a. Wang, *Front. Chem.*, 2020, **8**, 725.
5 M.-C. Tang, M.-Y. Chan and V. W.-W. Yam, *Chem. Rev.*, 2021, **121**, 7249–7279.
6 T.-T. Bui, F. Goubard, M. Ibrahim-Ouali, D. Gigmes and F. Dumur, *Beilstein J. Org. Chem.*, 2018, **14**, 282–308.
7 W.-P. To, G. Cheng, G. S. M. Tong, D. Zhou and C.-M. Che, *Front. Chem.*, 2020, **8**, 653.
8 C. C. Au-Yeung, L.-K. Li, M.-C. Tang, S.-L. Lai, W.-L. Cheung, M. Ng, M.-Y. Chan and V. W.-W. Yam, *Chem. Sci.*, 2021, **12**, 9516–9527.
9 L.-K. Li, C. C. Au-Yeung, M.-C. Tang, S.-L. Lai, W.-L. Cheung, M. Ng, M.-Y. Chan and V. W.-W. Yam, *Mater. Horiz.*, 2022, **9**, 281–293.
10 C.-Y. Wong, M.-C. Tang, L.-K. Li, M.-Y. Leung, W.-K. Tang, S.-L. Lai, W.-L. Cheung, M. Ng, M.-Y. Chan and V. W.-W. Yam, *Chem. Sci.*, 2022, **13**, 10129–10140.
11 M.-C. Tang, M.-Y. Leung, S.-L. Lai, M. Ng, M.-Y. Chan and V. W.-W. Yam, *J. Am. Chem. Soc.*, 2018, **140**, 13115–13124.
12 M.-Y. Leung, M.-C. Tang, W.-L. Cheung, S.-L. Lai, M. Ng, M.-Y. Chan and V. W.-W. Yam, *J. Am. Chem. Soc.*, 2020, **142**, 2448–2459.
13 S. K. Jeon, H. L. Lee, K. S. Yook and J. Y. Lee, *Adv. Mater.*, 2019, **31**, 1803524.
14 M. A. El-Sayed, *J. Chem. Phys.*, 1963, **38**, 2834–2838.
15 F. B. Dias, J. Santos, D. R. Graves, P. Data, R. S. Nobuyasu, M. A. Fox, A. S. Batsanov, T. Palmeira, M. N. Berberan-Santos, M. R. Bryce and A. P. Monkman, *Adv. Sci.*, 2016, **3**, 1600080.
16 M. K. Etherington, J. Gibson, H. F. Higginbotham, T. J. Penfold and A. P. Monkman, *Nat. Commun.*, 2016, **7**, 13680.
17 J. Gibson, A. P. Monkman and T. J. Penfold, *ChemPhysChem*, 2016, **17**, 2956–2961.
18 C. M. Marian, *J. Phys. Chem. C*, 2016, **120**, 3715–3721.
19 T. Hosokai, H. Matsuzaki, H. Nakanotani, K. Tokumaru, T. Tsutsui, A. Furube, K. Nasu, H. Nomura, M. Yahiro and C. Adachi, *Sci. Adv.*, 2017, **3**, e1603282.
20 I. Lyskov and C. M. Marian, *J. Phys. Chem. C*, 2017, **121**, 21145–21153.
21 P. K. Samanta, D. Kim, V. Coropceanu and J.-L. Brédas, *J. Am. Chem. Soc.*, 2017, **139**, 4042–4051.
22 H. Noda, H. Nakanotani and C. Adachi, *Sci. Adv.*, 2018, **4**, eaao6910.
23 Y. Wada, H. Nakagawa, S. Matsumoto, Y. Wakisaka and H. Kaji, *Nat. Photonics*, 2020, **14**, 643–649.
24 S.-T. Lam, N. Zhu and V. W.-W. Yam, *Inorg. Chem.*, 2009, **48**, 9664–9670.
25 X. He and V. W.-W. Yam, *Org. Lett.*, 2011, **13**, 2172–2175.
26 C.-T. Poon, W. H. Lam and V. W.-W. Yam, *J. Am. Chem. Soc.*, 2011, **133**, 19622–19625.
27 C.-T. Poon, W. H. Lam, H.-L. Wong and V. W.-W. Yam, *Chem.–Eur. J.*, 2015, **21**, 2182–2192.
28 H. Lee, D. Karthik, R. Lampande, J. H. Ryu and J. H. Kwon, *Front. Chem.*, 2020, **8**, 373.
29 I. S. Park, M. Yang, H. Shibata, N. Amanokura and T. Yasuda, *Adv. Mater.*, 2022, **34**, 2107951.
30 T. Fan, Y. Zhang, L. Wang, Q. Wang, C. Yin, M. Du, X. Jia, G. Li, D. Zhang and L. Duan, *Angew. Chem., Int. Ed.*, 2022, **61**, e202213585.
31 K. Stavrou, S. Madayanad Suresh, D. Hall, A. Danos, N. A. Kukhta, A. M. Z. Slawin, S. Warriner, D. Beljonne, Y. Olivier and A. Monkman, *Adv. Opt. Mater.*, 2022, **10**, 2200688.
32 S. Madayanad Suresh, L. Zhang, D. Hall, C. Si, G. Ricci, T. Matulaitis, A. M. Z. Slawin, S. Warriner, Y. Olivier, I. D. W. Samuel and E. Zysman-Colman, *Angew. Chem., Int. Ed.*, 2023, **62**, e202215522.
33 I. S. Park, M. Numata, C. Adachi and T. Yasuda, *Bull. Chem. Soc. Jpn.*, 2016, **89**, 375–377.
34 I. S. Park, K. Matsuo, N. Aizawa and T. Yasuda, *Adv. Funct. Mater.*, 2018, **28**, 1802031.
35 K. Matsuo and T. Yasuda, *Chem. Commun.*, 2019, **55**, 2501–2504.
36 J. H. Maeng, D. H. Ahn, H. Lee, J. Y. Lee and J. H. Kwon, *Dig. Tech. Pap.–SID Int. Symp.*, 2019, **50**, 363–366.
37 D. H. Ahn, S. W. Kim, H. Lee, I. J. Ko, D. Karthik, J. Y. Lee and J. H. Kwon, *Nat. Photonics*, 2019, **13**, 540–546.
38 H. Hirai, K. Nakajima, S. Nakatsuka, K. Shiren, J. Ni, S. Nomura, T. Ikuta and T. Hatakeyama, *Angew. Chem., Int. Ed.*, 2015, **54**, 13581–13585.
39 B. M. Bell, T. P. Clark, T. S. De Vries, Y. Lai, D. S. Laitar, T. J. Gallagher, J.-H. Jeon, K. L. Kearns, T. McIntire, S. Mukhopadhyay, H.-Y. Na, T. D. Paine and A. A. Rachford, *Dyes Pigm.*, 2017, **141**, 83–92.
40 C.-T. Poon, W. H. Lam, H.-L. Wong and V. W.-W. Yam, *J. Am. Chem. Soc.*, 2010, **132**, 13992–13993.
41 H.-L. Wong, W.-T. Wong and V. W.-W. Yam, *Org. Lett.*, 2012, **14**, 1862–1865.
42 Z. Yin, A. Y.-Y. Tam, K. M.-C. Wong, C.-H. Tao, B. Li, C.-T. Poon, L. Wu and V. W.-W. Yam, *Dalton Trans.*, 2012, **41**, 11340–11350.
43 C.-T. Poon, W. H. Lam and V. W.-W. Yam, *Chem.–Eur. J.*, 2013, **19**, 3467–3476.

44 C.-T. Poon, D. Wu, W. H. Lam and V. W.-W. Yam, *Angew. Chem., Int. Ed.*, 2015, **54**, 10569–10573.
45 C.-T. Poon, D. Wu and V. W.-W. Yam, *Angew. Chem., Int. Ed.*, 2016, **55**, 3647–3651.
46 B. Y.-W. Wong, H.-L. Wong, Y.-C. Wong, M.-Y. Chan and V. W.-W. Yam, *Chem.–Eur. J.*, 2016, **22**, 15095–15106.
47 C.-L. Wong, C.-T. Poon and V. W.-W. Yam, *Chem.–Eur. J.*, 2016, **22**, 12931–12940.
48 H. Chan, H.-L. Wong, M. Ng, C.-T. Poon and V. W.-W. Yam, *J. Am. Chem. Soc.*, 2017, **139**, 7256–7263.
49 C.-L. Wong, C.-T. Poon and V. W.-W. Yam, *Organometallics*, 2017, **36**, 2661–2669.
50 P. Li, H. Chan, S.-L. Lai, M. Ng, M.-Y. Chan and V. W.-W. Yam, *Angew. Chem., Int. Ed.*, 2019, **58**, 9088–9094.
51 P. Li, Q. Liang, E. Y.-H. Hong, C.-Y. Chan, Y.-H. Cheng, M.-Y. Leung, M.-Y. Chan, K.-H. Low, H. Wu and V. W.-W. Yam, *Chem. Sci.*, 2020, **11**, 11601–11612.
52 T. H.-C. Fung, C.-L. Wong, W.-K. Tang, M.-Y. Leung, K.-H. Low and V. W.-W. Yam, *Chem. Commun.*, 2022, **58**, 4231–4234.
53 D. Li, H. Zhang and Y. Wang, *Chem. Soc. Rev.*, 2013, **42**, 8416–8433.
54 M. L. Daly, C. A. DeRosa, C. Kerr, W. A. Morris and C. L. Fraser, *RSC Adv.*, 2016, **6**, 81631–81635.
55 Y.-J. Shiu, Y.-C. Cheng, W.-L. Tsai, C.-C. Wu, C.-T. Chao, C.-W. Lu, Y. Chi, Y.-T. Chen, S.-H. Liu and P.-T. Chou, *Angew. Chem., Int. Ed.*, 2016, **55**, 3017–3021.
56 G. Li, W. Lou, D. Wang, C. Deng and Q. Zhang, *ACS Appl. Mater. Interfaces*, 2019, **11**, 32209–32217.
57 G. Li, F. Zhan, W. Lou, D. Wang, C. Deng, L. Cao, Y. Yang, Q. Zhang and Y. She, *J. Mater. Chem. C*, 2020, **8**, 17464–17473.
58 H. Wang, C. Cheng, D. Wang, W. Lou, Y. Zhu, C. Deng, G. Li and Q. Zhang, *Org. Electron.*, 2021, **96**, 106254.
59 T. A. Enache and A. M. Oliveira-Brett, *J. Electroanal. Chem.*, 2011, **655**, 9–16.
60 J. Almond-Thynne, D. C. Blakemore, D. C. Pryde and A. C. Spivey, *Chem. Sci.*, 2017, **8**, 40–62.
61 L.-S. Cui, H. Nomura, Y. Geng, J. U. Kim, H. Nakanotani and C. Adachi, *Angew. Chem., Int. Ed.*, 2017, **56**, 1571–1575.
62 J. Guo, J. Fan, L. Lin, J. Zeng, H. Liu, C.-K. Wang, Z. Zhao and B. Z. Tang, *Adv. Sci.*, 2019, **6**, 1801629.
63 H. Liu, S. Song, H. Chen, Z. Zhao, G. Xie and B. Z. Tang, *Org. Electron.*, 2021, **99**, 106339.
64 R. J. Vázquez, J. H. Yun, A. K. Muthike, M. Howell, H. Kim, I. K. Madu, T. Kim, P. Zimmerman, J. Y. Lee and T. G. Iii, *J. Am. Chem. Soc.*, 2020, **142**, 8074–8079.
65 L. Wang, I. S. Tamgho, L. A. Crandall, J. J. Rack and C. J. Ziegler, *Phys. Chem. Chem. Phys.*, 2015, **17**, 2349–2351.
66 R. J. Vázquez, H. Kim, P. M. Zimmerman and T. Goodson, *J. Mater. Chem. C*, 2019, **7**, 4210–4221.
67 H. Kim, B. Keller, R. Ho-Wu, N. Abeyasinghe, R. J. Vázquez, T. Goodson and P. M. Zimmerman, *J. Am. Chem. Soc.*, 2018, **140**, 7760–7763.
68 L. Bergmann, G. J. Hedley, T. Baumann, S. Bräse and I. D. W. Samuel, *Adv. Sci.*, 2016, **2**, e1500889.
69 K. Hoshi, M. Itaya, K. Tahara, A. Matsumoto, A. Tabata, H. Nagamune, Y. Yoshida, E. Hase, T. Minamikawa, T. Yasui, T. Katayama, A. Furube, K. Minagawa, Y. Imada and F. Yagishita, *RSC Adv.*, 2021, **11**, 26403–26407.
70 Y. Hou, T. Biskup, S. Rein, Z. Wang, L. Bussotti, N. Russo, P. Foggi, J. Zhao, M. Di Donato, G. Mazzone and S. Weber, *J. Phys. Chem. C*, 2018, **122**, 27850–27865.
71 L.-S. Cui, A. J. Gillett, S.-F. Zhang, H. Ye, Y. Liu, X.-K. Chen, Z.-S. Lin, E. W. Evans, W. K. Myers, T. K. Ronson, H. Nakanotani, S. Reineke, J.-L. Bredas, C. Adachi and R. H. Friend, *Nat. Photonics*, 2020, **14**, 636–642.
72 I. Kim, S. O. Jeon, D. Jeong, H. Choi, W.-J. Son, D. Kim, Y. M. Rhee and H. S. Lee, *J. Chem. Theory Comput.*, 2020, **16**, 621–632.
73 S.-B. Ko, S. Kang and T. Kim, *Chem.–Eur. J.*, 2020, **26**, 7767–7773.